Journal of Materials Chemistry A

An insight into the electrochemical performance of La0.5-xPrxBa0.5CoO3-δ as cathodes for solid oxide fuel cells: study of the O2-reduction reaction.

Journal:	*Journal of Materials Chemistry A*
Manuscript ID	TA-ART-05-2018-004338.R1
Article Type:	Paper
Date Submitted by the Author:	31-Jul-2018
Complete List of Authors:	Garces, Diana; Centro Atomico Constituyentes, Wang, Hongqian; Northwestern University, Materials Science and Engineering Barnett, Scott; Northwestern University, Materials Science and Engineering Leyva, Ana; Centro Atómico Constituyentes, Departamento de Física Napolitano, Federico; Centro Atomico Bariloche, Departamento Caracterizacion de Materiales; Consejo Nacional de Investigaciones Cientificas y Tecnicas Fuentes, Rodolfo; Comision Nacional de Energia Atomica, Centro Atomico Constituyentes-Instituto de Nanociencia y Nanotecnologia; Consejo Nacional de Investigaciones Cientificas y Tecnicas Troiani, Horacio; Centro Atomico Bariloche, Caracterización de Materiales Mogni, Liliana; CONICET, Centro Atomico Bariloche; Comision Nacional de Energia Atomica, Instituto de Nanociencia y Nanotecnologia

Journal of Materials Chemistry A

ARTICLE

An insight into the electrochemical performance of $La_{0.5-x}Pr_xBa_{0.5}CoO_{3-\delta}$ as cathodes for solid oxide fuel cells: study of the O_2-reduction reaction.

Received 00th January 20xx,
Accepted 00th January 20xx

DOI: 10.1039/x0xx00000x

www.rsc.org/

D. Garcés [a], H. Wang [b], S. A. Barnett [b], A. G. Leyva [a,c], F. Napolitano [d,e], R. O. Fuentes [a,e], H. Troiani [d,e], L.V. Mogni*[,d,e]

New LT-SOFC cathodes with $La_{0.5-x}Pr_xBa_{0.5}CoO_{3-\delta}$ ($0 \le x \le 0.5$) compositions were studied. The La-rich compounds exhibit an inter-growing cubic and tetragonal structure whereas the Pr-rich show a tetragonal structure. Cathode polarization resistances, estimated from electrochemical impedance (EIS), take values around 0.15 and 0.04 Ωcm^2 in air at 600 and 700 ºC, respectively. The O_2-reduction mechanism and its kinetic coefficients, O-ion diffusion (D_{chem}) and O-surface exchange (k_{chem}), were studied by applying the ALS model for macro homogenous porous electrodes to the EIS data, in combination with microstructural parameters obtained from three-dimensional tomography using focused ion beam–scanning electron microscopy (3D FIB-SEM). The diffusion coefficients for samples with mixing of phases take values of D_{chem} ~10^{-6} cm^2/s, at 700 ºC in air, whereas the pure tetragonal phases present lower values D_{chem} ~10^{-8} cm^2/s. On the contrary the k_{chem} for all samples takes values ranging between 0.4 and 1.10^{-4} cm/s at 700 ºC in air. In addition, the origin of time evolution of polarization at 700 °C in air was evaluated by combining the EIS spectra as a function of time and the ex-situ sample characterization of fresh and tested samples by 3D FIB-SEM tomography and inductively coupled plasma-optical emission spectrometry (ICP-OES). Little changes of microstructures were detected, whereas an increasing of the amount of a water-soluble Ba surface species in comparison with total cation surface segregation was observed for all samples after the ageing. This may constitute the main reason causing the polarization resistance degradation. However, the analysis of time evolution shows, that contrary to the situations reported for SrO segregation in Sr-based perovskites, the D_{chem} is the coefficient mainly affected for compositions with inter-grown phases. At the same time, both D_{chem} and k_{chem} decreases with time when only the tetragonal phase is present.

Introduction

The large-scale commercialization of SOFCs is currently constrained by a combination of cost and durability issues. In order to address these concerns, much effort has been focused on developing low-temperature SOFCs (LT-SOFCs), with cell operating temperature < 700 °C [1]. One of the major concerns to achieve this goal is the development of cathode materials with low polarization resistance and good stability over time.

Cobaltites with the perovskite structure such as, the Strontium-Barium cobaltites $Ba_{0.5}Sr_{0.5}Co_{0.8}Fe_{0.2}O_{3-\delta}$(BSCF) [2], are promising cathode materials for LT-SOFCs. Despite the good performance of Sr-containing perovskites, a significant problem is the long-term instability due to Sr-surface segregation [3]. Yildiz's group pointed out, from the study of thin film electrodes, that the cation surface segregation increases due to the size mismatch between the dopant and host cations, being more important the Ba surface segregation than Sr and Ca surface enrichment for (La,M)MnO_3 with M = Ba, Sr or Ca electrodes [4]. However, there is not enough information about Ba-segregation in Ba-cobaltites porous electrodes. In these perovskites, the Ba plays a key role since its large cation radii mismatch also distorts the cubic crystal structure promoting the oxygen vacancy formation and migration [5], thus reducing the $R_{c,p}$ due to the improvement of the O-surface exchange and the O-ion diffusion. However, the same structural distortion, also induces a slow segregation of a hexagonal perovskite phase [6–8] which deteriorates the O_2 reduction kinetics with time [9]. Recent works have shown that $La_{0.5}Ba_{0.5}CoO_{3-\delta}$ is a promising cathode material for LT-SOFCs because of its low cathode polarization resistance [10–12]. Besides, in this oxide we did not observe the hexagonal phase formation suggesting that La^{3+} ions plays an important role in stabilizing the cubic phase because of its charge and ionic radii.

With these ideas, in this work, the La content of the perovskite oxide $La_{0.5}Ba_{0.5}CoO_{3-\delta}$ is partially substituted with Pr as $La_{0.5-x}Pr_xBa_{0.5}CoO_{3-\delta}$ (LPBC), with $0 \le x \le 0.5$ to improve even more the cathode performance mainly due to the property of the Pr of having double valence (Pr^{3+} and Pr^{4+}). It was observed that the Pr substitution in CeO_2 based oxides improves the electric conductivity, added to the fact that the reduced size of this cation favors the

[a] CNEA, Centro Atómico Constituyentes-Instituto de Nanociencia y Nanotecnología, San Martin B1650KNA, Argentina.
[b] Northwestern University, Department of Materials Science and Engineering, Evanston60208, USA.
[c] ECyT-UNSAM, San MartinB1650KNA, Argentina.
[d] CNEA, Centro Atómico Bariloche-Instituto de Nanociencia y Nanotecnología, S. C. de Bariloche 8400, Argentina.
[e] CONICET, Godoy Cruz 2290 (C1425FQB) CABA - Argentina
*Email - mogni@cab.cnea.gov.ar
Electronic Supplementary Information (ESI) available: [details of any supplementary information available should be included here]. See DOI: 10.1039/x0xx00000x

formation of oxygen vacancies that improving the ionic conductivity [13-15]. Therefore, it is expected that Pr will play a similar role in LPBC perovskite-type oxides. Samples synthesized at 1000℃ exhibit a combination of cubic and tetragonal symmetry for $x \leq 0.1$, whereas above this value the cation ordering produces a layering structure with tetragonal symmetry. The Electrochemical Impedance Spectroscopy (EIS) as a function of temperature (T), oxygen partial pressure (pO_2) and time, in combination with 3D focused ion beam-scanning electron microscopy (FIB-SEM) tomography and the inductively coupled plasma-optical emission spectrometry (ICP-OES) studies, were used to analyze the mechanisms of O_2 reduction reaction and electrode degradation with time.

Experimental

Powders with nominal composition $La_{0.5-x}Pr_xBa_{0.5}CoO_{3-\delta}$ (LPBC) were synthesized via a combined EDTA-citrate complexing sol-gel process. Stoichiometric amounts of $La(NO_3)_3{\cdot}6H_2O$, $Ba(NO_3)_2$, $Co(NO_3)_3{\cdot}6H_2O$ and $Pr(NO_3)_2{\cdot}xH_2O$ were dissolved into a EDTA-$NH_3{\cdot}H_2O$ solution (pH ≈ 6) under heating and stirring conditions. A proper amount of citric acid-$NH_3{\cdot}H_2O$ solution (pH ≈ 6) was added at a mole ratio of 1:1:2 for EDTA: total metal ions: citric acid. The mixed solution was firstly evaporated at 80 ºC to form a red transparent gel and then heated at 150 ºC for several hours to obtain a dark dry foam structure. After decomposition on a hot plate, the powders were calcined at 400 ºC (4 h, in air) and then at 1000 ºC (4 h, in air). Each sample of the LPBC series was labeled according to its corresponding lanthanum content, i.e., La30 represents the $La_{0.30}Pr_{0.20}Ba_{0.50}CoO_{3-\delta}$ compound.

The crystal structure was studied by X-ray diffraction at the D10B-XPD beamline of the LNLS (Brazilian Synchrotron Light Laboratory, Campinas, Brazil) in static air at room temperature by using the high resolution mode with a Cyberstar detector, a Ge(111) crystal analyzer and a Si(111) monocromator. The wavelength was set at 1.5495(4) Å. Data in the angular region of 2θ 20 – 90º were collected at room temperature in a step-scanning mode, with a step length of 0.02 and a step-counting time of 3 s.

Sample nanostructures were also studied by Transmission Electron Microscopy (TEM) with a Philips CM 200 UT (LaB6 gun) and a TECNAI F-20 (FEG) microscopes. HR-TEM images and Selected Area Electron Diffraction (SAED) patterns were obtained and compared to simulated patterns/HR-TEM images. Simulations were performed with the software JEMS (Java versionV3-3526U2008s, CIME-EPFL), using structural parameters obtained from the Rietveld analyses.

Oxygen content (3-δ) vs. temperature and isothermal measurements of the equilibrium pO_2 vs. 3-δ were performed using highly sensitive thermogravimetric equipment [16], consisting of a symmetrical thermobalance based on a Cahn 1000 electrobalance coupled to an electrochemical gas blending system[17]. The oxygen content was determined by in situ reduction in dry H_2 at 1000 °C considering La_2O_3, Pr_2O_3, BaO, and Co as final products (checked by XRD). The sample mass was measured in air with a rate of 5°C/min in the range of 20–800°C. The equilibrium pO_2 isotherms were measured at 600 and 700 ºC within the pO_2 ranges 1×10^{-2} atm ≤ pO_2 ≤ 1 atm.

Electrochemical characterization was performed by Electrochemical Impedance Spectrometry (EIS) in symmetrical cell configuration (LPBC/GDC/LPBC) by using an AUTOLAB PGSTAT30 (EcoChemie) potentiostat coupled to a FRA2 analyzer. The symmetrical cells consisted of a dense $Ce_{0.9}Gd_{0.1}O_{1.95}$ (GDC, Fuel Cell Materials) electrolyte (area ~0.8 cm², thickness ~0.1 cm), where firstly a porous layer of GDC and afterwards a porous layer of the LPBC were deposited consecutively on both sides of the GDC pellets by spin coating. The inks were prepared by mixing the corresponding ceramic powders (GDC or LPBC) with ethanol, α-terpineol (≥96%, Sigma Aldrich), polyvinyl butyral (Sigma Aldrich), and polyvinyl pyrrolidone (Sigma Aldrich) in a 40:40:27:2:1 mass ratio. The porous layer of GDC improves the adherence of LPBC cathode onto the GDC dense electrolyte [18]. After deposition, the porous GDC layer was heat treated at 1400ºC during 1 h in air, while the LPBC porous electrode was heat treated at 1000 ºC 1 h in air. The EIS measurements for all samples were carried out in synthetic air in a temperature range between 400 and 800 ºC. At 600 and 700 ºC the EIS spectra were collected varying the oxygen partial pressure (pO_2) between 1 and 5.10^{-3} atm by using a home-made device to test symmetrical cells coupled to an electrochemical oxygen pump and sensor. In addition, EIS spectra were also collected at 0.2 and 0.05 atm varying the temperature, with 50 ºC step, between 500 and 800 ºC. Life testing was performed at 700ºC in air during 400 hours for La00, La30, La35 and La50 samples.

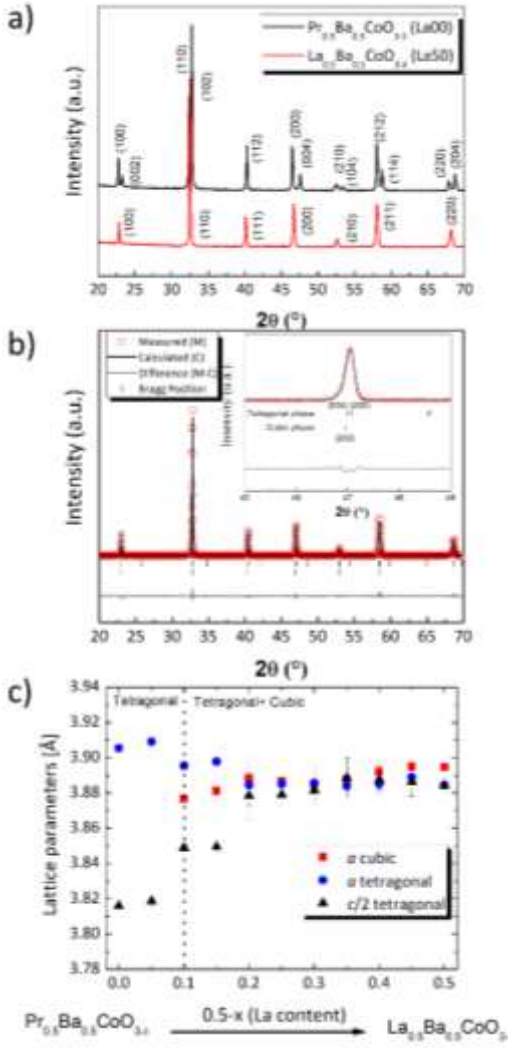

Figure 1: a) XRD patterns of La00 and La50 samples .b) XRD pattern fitting for La30 sample (χ^2 = 2.57, Rp = 16.9 and Rwp = 20.4). The angular range of 45-49° is shown for a better understanding. c) Variation of cubic (a = b = c) and pseudo cubic (a = b, c'= c/2 for tetragonal) lattice parameters with the lanthanum content (0.5-x) for $La_{0.5-x}Pr_xBa_{0.5}CoO_{3-\delta}$.

The electrode microstructures were characterized by Field Emission Gun Scanning Electron Microscopy (FEG-SEM) with a FEI Nova NANO 230 microscope. The GDC porous layer and the electrode thicknesses are around ~5-10 µm and ~12–15 µm, respectively. Samples before (Fresh) and after (Tested) aging test were prepared for FIB-SEM tomographic analysis by fracturing, epoxy infiltration and polishing. Serial sectioning was done on a FEI Helios. Backscattered electron (BSE) detector with an accelerating voltage of 2 kV was used to obtain good contrast between the solid and pore phases. Microstructural parameters including porosity, tortuosity, surface area and particle size distribution were then calculated based on the 3D data.

ICP-OES analysis was also done using a Thermo Scientific iCAP 7600 spectrometer on the fresh and post-tested samples to examine possible changes in the cation surface segregation. The samples were fractured into three fragments and stirred in ultrapure H_2O for 10 min, followed by transferring the samples into a 12 mol·L^{-1}HCl solution and stirring until the electrodes were completely dissolved. The ultrapure H_2O and the concentrated HCl solutions were mixed with the appropriate amounts of H_2O/HCl/HNO_3 to yield 0.36 mol·L^{-1}HCl/0.72 mol·L^{-1} HNO_3 solutions for ICP-OES injection. A certified stock solution (10.00 µg/mL from Inorganic Ventures) containing La, Pr, Ba and Co was used to prepare the calibration standards for quantification. The following background corrected emission lines were chosen for evaluation: La (379.478 nm; 412.323 nm), Pr (414.311 nm; 417.939 nm; 422.535 nm), Ba (233.527 nm; 455.403 nm; 493.409 nm), Co (228.616 nm; 237.862 nm).

Results and Discussion

Structure and microstructure characterization

Figure 1.a) shows the XRD pattern of La50 and La00 samples where the Bragg index of each peak was included in the graphic. At first glance, XRD data of La50 sample could be indexed as a cubic perovskite (space group $Pm\bar{3}m$), however a peak splitting on La00 indicates the formation of a tetragonal phase (space group $P4/mmm$). As La content increases, the peaks of the tetragonal phase collapse to a unique broader and distorted peak. The XRD patterns were refined by the Rietveld method with different structural models, including the possibility of a cubic or a tetragonal phase with higher distortion levels, as well as a combination of both cubic and tetragonal phases. The best refinements (see Figure 1.b)) were obtained for a combination of the two phases. Figure 1.b) shows, as an example, the measured data, the calculated and the difference between them for La30 sample. The inset of Figure 1.b) illustrates with more details an example of the peak asymmetries observed in the diffraction patterns due to the overlapping of the Bragg reflections from both phases. The Rietveld refinements considering a mix of phases were also performed from different sets of initial parameters obtaining similar goodness of fit, independently of the initial seed (average values for fitting parameters are χ^2~ 2.7, R_p ~26.7 and R_{wp} ~19.4). The average results indicate that the La00 and La05 samples exhibit tetragonal symmetry, whereas all the other compositions present between 30-50% of cubic phase and 70-50% of tetragonal phase. The evolution of the pseudo cubic lattice parameters (a = b = c for $Pm\bar{3}m$ a = b ≈ c/2 for $P4/mmm$) with La content is shown in Figure 1.c). As it can be observed from this figure the samples with high La content (La ≥ 0.20) are a mix of cubic and tetragonal phase with small differences in the lattice parameters. The presence of two phases was confirmed by HR-TEM, where Figure 2.a) shows how La45 sample exhibits zones with the typical layered ordering of tetragonal structure, which become smoothly to the cubic structure with a perfect match between the lattice parameters, in agreement with those observed by XRD (see Figure 2.a - circles amplified areas with typical tetragonal and cubic structures). As the La content decreases, samples tend to be more "tetragonal" with a largest separation of the pseudo cubic lattice parameter between the cubic and tetragonal phases. Figure 2.b) and c) show a HR-TEM images of La15 sample and its electron diffraction pattern, which can be indexed as tetragonal phase with pseudo cubic lattice parameter of $a = b = 3.9 \pm 0.2$ Å and $c/2 = 3.9 \pm 0.2$ Å which are in agreement with those obtained from XRD Rietveld refinements.

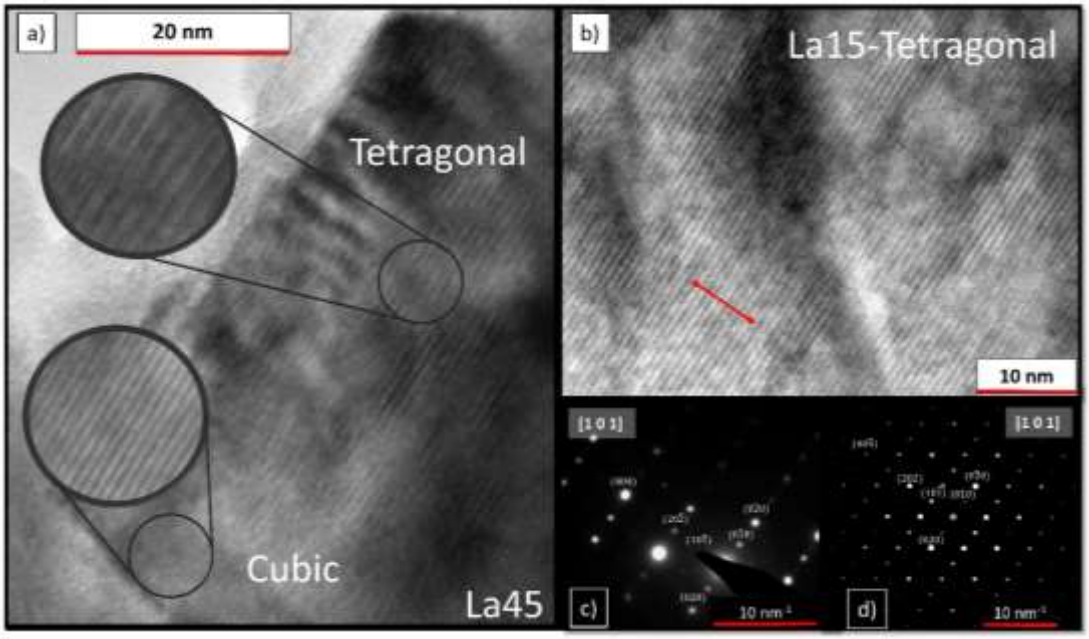

Figure 2: a) and b) HR-TEM image for La45 and La15 sample, respectively. Comparison electron diffraction pattern (c) of the area shown in HR-TEM image b) and kinematical simulation (d) for SAED pattern along the $[101]_T$ ZA.

Figure 3.a) and b) are SEM images showing cross sectional and electrode surface views of the symmetrical cell La35/GDC/La35, respectively. Figure 3.c) and d) illustrate 2D FIB-SEM cross-sectional images of the La35-fresh and tested sample, respectively. The bright phase represents the particles and the dark phase are the epoxy-infiltrated pores. The corresponding 3D reconstructed structures of electrode porous layer of the La35-fresh and tested samples are shown in Figure 3.e) and f), note that the GDC porous layer was ignored for the tomography analysis. The structure is typical of SOFC cathode electrodes produced by firing of particle compacts, showing reasonable uniform particle sizes and good necking between particles.

Figure 3: SEM images of La35 symmetrical cell, a) cross and b) top section. Typical 2D FIB-SEM cross-sectional image of c) La35-fresh and d) La35-tested with pore phase infiltrated by epoxy. The corresponding 3D reconstruction of e) La35-fresh and f) La35-tested with LPBC particles shown in green and pores transparent. Note that the 3D view only shows the electrode region. g) Cumulative particle size distribution of LPBC calculated from obtained 3D data sets.

indicates the microstructural parameters: solid phase fraction (ε), solid phase and pore phase tortuosity (τ_s,τ_p), specific surface area (*a*) and the mean particle size determined from the analysis of the 3D data and the cumulative particle size distribution (Figure 3.g) of La35 before and after life testing.

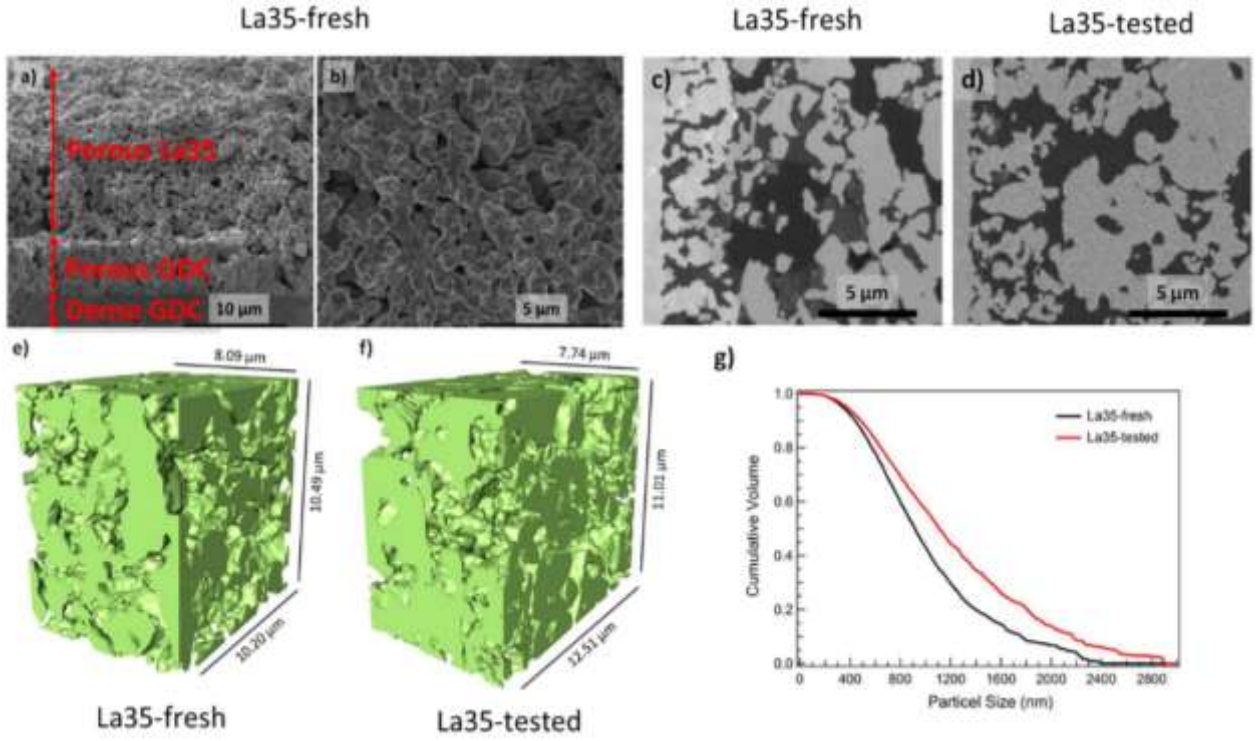

Figure 3: SEM images of La35 symmetrical cell, a) cross and b) top section. Typical 2D FIB-SEM cross-sectional image of c) La35-fresh and d) La35-tested with pore phase infiltrated by epoxy. The corresponding 3D reconstruction of e) La35-fresh and f) La35-tested with LPBC particles shown in green and pores transparent. Note that the 3D view only shows the electrode region. g) Cumulative particle size distribution of LPBC calculated from obtained 3D data sets.

Table 1: Microstructural parameters for La35 porous electrode obtained from 3D FIB-SEM reconstruction.

Sample	solid phase fraction (ε)	solid phase tortuosity (τ_s)	pore phase tortuosity (τ_p)	specific surface area† (a)	mean particle size
La35 - fresh	52.4 %	1.28	1.22	3.78 μm^{-1}	900 nm
La35 - tested	53.7%	1.28	1.25	3.12 μm^{-1}	1100 nm

† the specific surface area is defined as the cathode area per volume unit.

Electrochemical Performance

The total cathode polarization resistances ($R_{C,P}$) obtained from the EIS measurements in air at 600 and 700 °C are presented in Figure 4. Regardless the La content, $R_{C,P}$ takes values between 0.07 and 0.22 Ωcm² at 600 °C and between 0.03 and 0.06 Ωcm² at 700 °C. These values are compared with some typical cubic perovskites (black lines) and double perovskites (red lines) cathodes resistances reported at literature. These figures show that the $R_{C,P}$ of $La_{0.5-x}Pr_xBa_{0.5}CoO_{3-\delta}$ are competitive with the best cathodes reported in the literature.

The $R_{C,P}$ values are the result of different cathode processes that can be separated in frequency by the impedance spectroscopy. As an example, Figure 5.b) and c) show impedance spectra, Nyquist and Bode plots (data points), measured at 600 ºC and pO_2 = 0.05 atm for the symmetrical cell La30/GDC/La30 and Figure 5.d) and e) show the same information at 700ºC. All spectra were normalized to the geometric area of the electrodes in the symmetrical cell configuration and show two arcs denoting the two different processes. Similar results were reported for Pr-free La-Ba cobaltite [10]. The two arcs are observed at temperatures above 600 °C, but

only one EIS arc is observed at lower temperature. All cathode compositions present similar behavior shown in Figure 5.

In order to study the mechanism of the O_2 reduction reaction (ORR), the electrochemical response was analyzed as a function of T and pO_2. The EIS spectra were fitted using the Electrical Equivalent Circuits (EEC) approximation. This circuit is composed by the inductance of connectors (L) and the electrolyte resistance ($R_{electrolyte}$), whereas the electrode response is fitted by the combination of a Gerischer for high frequency arc (Z_G) and a resistance (R_{LF}) in parallel with a capacitor (Cpe_{LF}) for the low frequency arc (Z_{LF}) (see Figure 5.a). The resulting fits show good agreement with the measured spectrum.

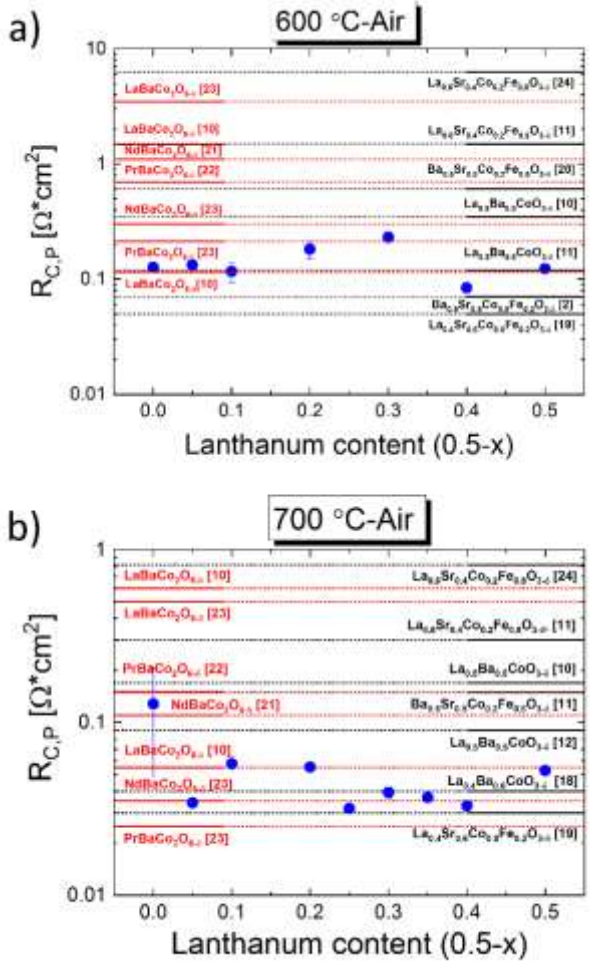

Figure 4: Total polarization resistance as a function of lanthanum content in air. Figures a) and b) compare the $R_{C,P}$ of $La_{0.5-x}Pr_xBa_{0.5}CoO_{3-\delta}$ at 600 and 700 °C, respectively, with other porous single phases cathodes with cubic (black lines) and tetragonal (red lines) symmetry [2,10–12,18-24].

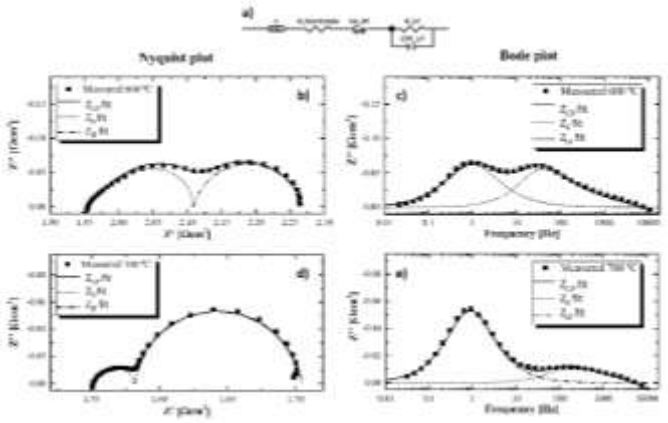

Figure 5: a) Electrical equivalent circuit (EEC) used for fitting the EIS spectra in the whole frequency range. b,d) Nyquist and c,e) Bode plot obtained for La30 sample in a pO_2 = 0.05 atm at 600 and 700ºC, respectively. Data point represents the measured data, solid line represents the arcs resulting of fitting data with the EEC proposed and dashed lines indicating the different contributions.

Figure 6.a) and b) show the log-log plot for the high frequency Gerischer resistance (R_G) and the low frequency resistance (R_{LF}) vs pO_2 for the La30 sample at 600 and 700 °C, respectively. The pO_2 dependences of R_G and R_{LF} fit approximately to $R_G \propto (pO_2)^{-0.25}$ and $R_{LF} \propto (pO_2)^{-1}$. Note that red lines show the estimation of polarization loss due to O_2 gas diffusion through a porous electrode with a 47.3% of porosity, $\boldsymbol{\tau_P}$ = 1.22 and length $\boldsymbol{l}$ = 15 μm modeled by considering both normal and Knudsen diffusion as reported in [25,26]. The R_{LF} values shows similar values, as well as the same pO_2 and temperature dependence, independently of cathode composition for the series $La_{0.5-x}Pr_xBa_{0.5}CoO_{3-\delta}$. This result is in agreement with none significant microstructural differences observed within the series. Figure 6.c) shows the Arrhenius plot of R_G and R_{LF} obtained from the fitting of EIS spectra collected as a function of T in air and pO_2 = 0.05 atm. The pO_2 = 0.05 atm was selected since as it is observed from Figure 5 the two arcs can be easily distinguished. Both process show markedly different activation energies. Whereas the R_G has an activation energy of ~ 1 eV, the O_2-gas diffusion is almost independent of T. These results suggest that the electrochemical response is limited by one or two mechanisms, depending on the conditions. At temperatures ≤ 600 ºC, the target T for low temperature SOFC [1], the high frequency contribution R_G associated with chemical processes co-limited by O-surface exchange and O-ion diffusion [25,27] is dominant. Whereas at higher temperatures (T > 700ºC) R_G becomes small enough, or at very low pO_2 the low frequency R_{LF} response increases being in both cases the O_2-gas diffusion the main responsible of the cathode polarization losses. However, the chemical process increases its impedance for Pr-rich compositions being comparable to the O_2 gas diffusion.

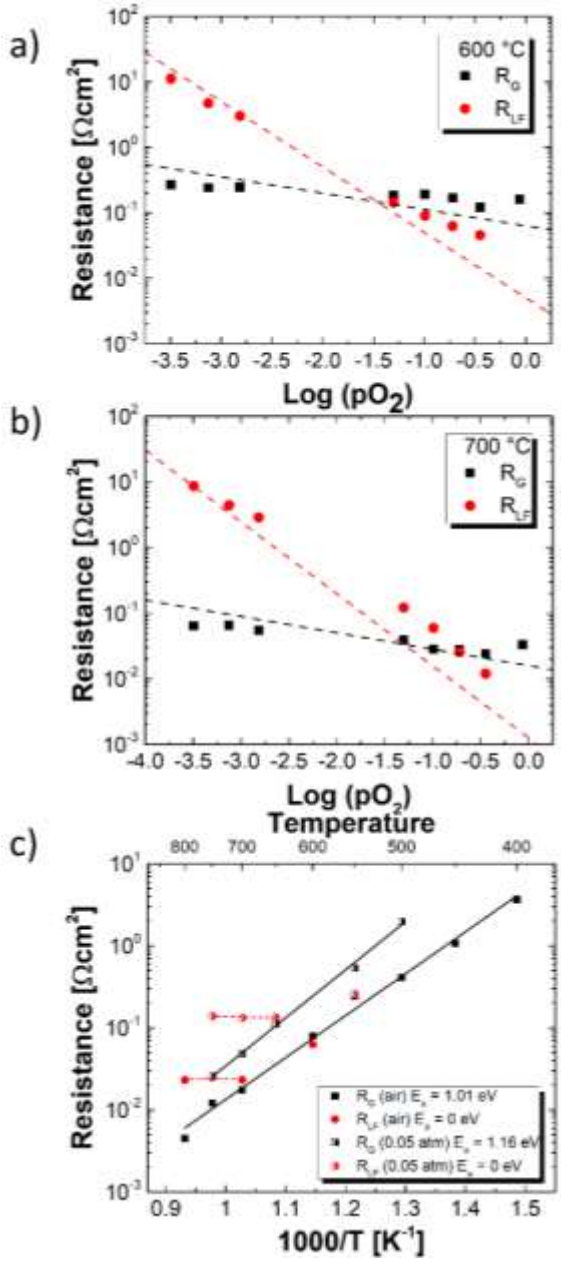

Figure 6: a) and b) Log-log plot of the high frequency Gerischer resistance (R_G) and the low frequency resistance (R_{LF}) with pO_2 at 600 and 700 °C for La30 sample. Dotted lines indicate the pO_2 dependences $R_G \propto (pO_2)^{-0.25}$ and $R_{LF} \propto (pO_2)^{-1}$. b) Arrhenius plot for the Gerischer resistance (R_G) and the low frequency resistance (R_{LF}) in air and pO_2 = 0.05 atm. The activation energies are indicated on the graphs.

The Gerischer type impedance $Z_G = R_G \frac{1}{\sqrt{1+j\omega\tau_G}}$ can be modeled by the Adler-Lane-Steel (ALS) models [27] mentioned before. In this model the resistance R_G and the time constant τ_G can be directly related to microstructural, thermodynamic and kinetic parameters by:

$$R_G = \frac{RT}{4F^2}\frac{1}{\sqrt{4a\Re_O c_O x_V^0 D_{ef}}} \quad (1)$$

$$\tau_G = \frac{(1-\varepsilon)c_O x_V^0}{4a\Re_O A_O} \quad (2)$$

where $\Re o$ is the oxygen molar equilibrium surface rate and D_{ef} is the effective diffusion coefficient of oxygen vacancies; c_O is the concentration of oxygen lattice sites involved in the diffusion mechanism, $x_V^0 = \delta_{eqb}/3$ is the molar fraction of oxygen vacancies at equilibrium and $A_O = -\frac{1}{2RT}\frac{\partial \mu_{O_2}}{\partial ln\delta}$ is the thermodynamic factor describing how oxygen non-stoichiometry varies with oxygen chemical potential in the case of O-vacancies defects. The microstructure of the electrode is considered explicitly through the electrode porosity ε and the electrode specific surface area *a*, whereas the MIEC-phase tortuosity factor τ is contained within $D_{ef} = \frac{(1-\varepsilon)}{\tau}\frac{D_{chem}}{A_O}$. The $\Re o$ surface exchange rate can show different pO_2 dependences, $\Re o = \frac{k_{chem}}{A_O} c_V p O_2^n$, where m values can takes values between 0 and 1 depending of the mechanism limiting surface reaction rate [28,29], c_V is molar the concentration of the O-vacancies and k_{chem} is the chemical surface reaction coefficient.

Then, the O-ion chemical diffusion ($\boldsymbol{D_{chem}}$) and chemical surface reaction coefficients ($\boldsymbol{k_{chem}}$) can be obtained by combining R_G and τ_G from the EIS fitted data as a function of T and pO_2, the microstructure parameters (ε, *a* and τ) from 3D-FIB-SEM tomography, and the O-vacancy concentration and A_O from TG data (3-δ vs T and pO_2, not show here). Figure 7 shows $\boldsymbol{D_{chem}}$, $\Re o$ and $\boldsymbol{k_{chem}}$ for all samples vs pO_2 at 700 ºC. Figure 7.a) shows the independence of $\boldsymbol{D_{chem}}$ with pO_2, which indicates a O-ion diffusion mechanism dominated by O-vacancies jumps in the bulk [27,30]. The tetragonal $Pr_{0.5}Ba_{0.5}CoO_{3-\delta}$ presents the lower values for $\boldsymbol{D_{chem}}$ (~10^{-8} cm^2/s for La00), one and two orders of magnitude lower than samples having a combination of cubic and tetragonal phases. This would indicate that the diffusive process present in these samples is favored with the cationic disorder. Contrary to $\boldsymbol{D_{chem}}$, the $\Re o$ shows a strong dependence with pO_2, with n between 0.3 and 0.8 (see Figure 7.b), which can be assigned to a surface process dominated by surface dissociation or surface dissociative adsorption according to Adler's model [28]. Figure 7.c) shows the $\boldsymbol{k_{chem}}$ obtained from $\Re o$ assuming m = 0.5. At difference that is observed for O-ion diffusion there is not an important difference between the $\boldsymbol{k_{chem}}$ obtained for sample with tetragonal phase from those with mixed of phases ($\boldsymbol{k_{chem}}$ ~ 0.4-2 10^{-4} cm/sat 700 ºC in air).

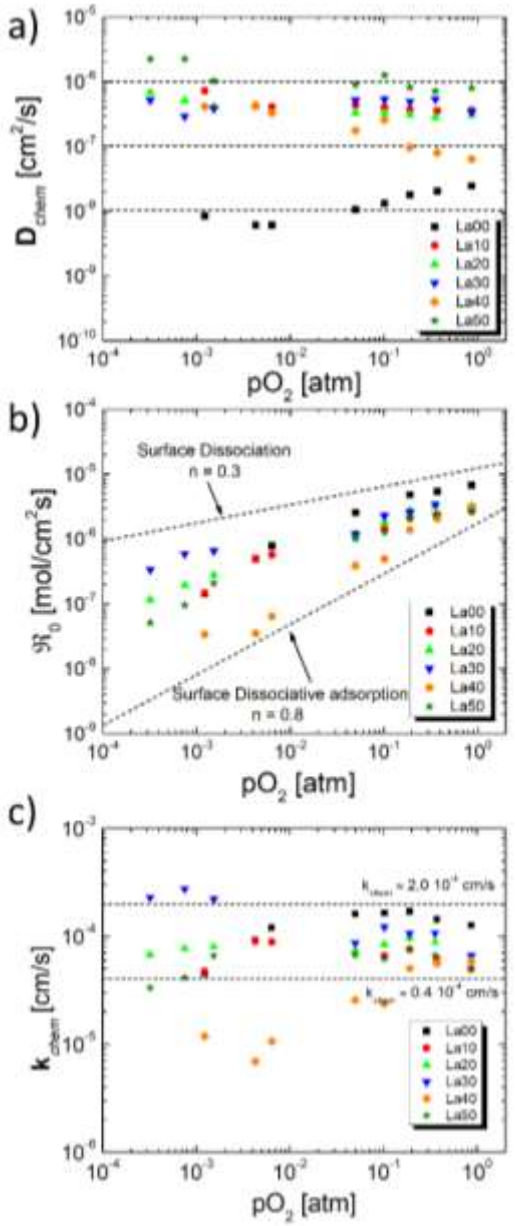

Figure 7: Kinetic parameters a) $\mathbf{D}_{chem}$, b) $\Re o$ and c) $\mathbf{k}_{chem}$ obtained from the fittin of EIS data vs pO_2 at 700 ºC by using the ALS mode for all samples.

The activation energy for $\boldsymbol{D}_{chem}$ (and $\Re o$) obtained from Figure 8.a (and 8.b) suggests a substantial difference between the pure tetragonal $Pr_{0.5}Ba_{0.5}CoO_{3-\delta}$ and the other samples with mixed phases. Thus, for La00 the activation energy for $\boldsymbol{D}_{chem}$ is higher (~1.1 eV) than the other samples (~ 0.7 eV), whereas the contrary is observed for $\Re o$ with an activation energy of ~ 0.9 eV, lower than the value of ~1.3 eV observed for the other compounds.

Table 2 shows $\boldsymbol{D}_{chem}$ and $\boldsymbol{k}_{chem}$ at 600 and 700 °C as well as its activation energies.

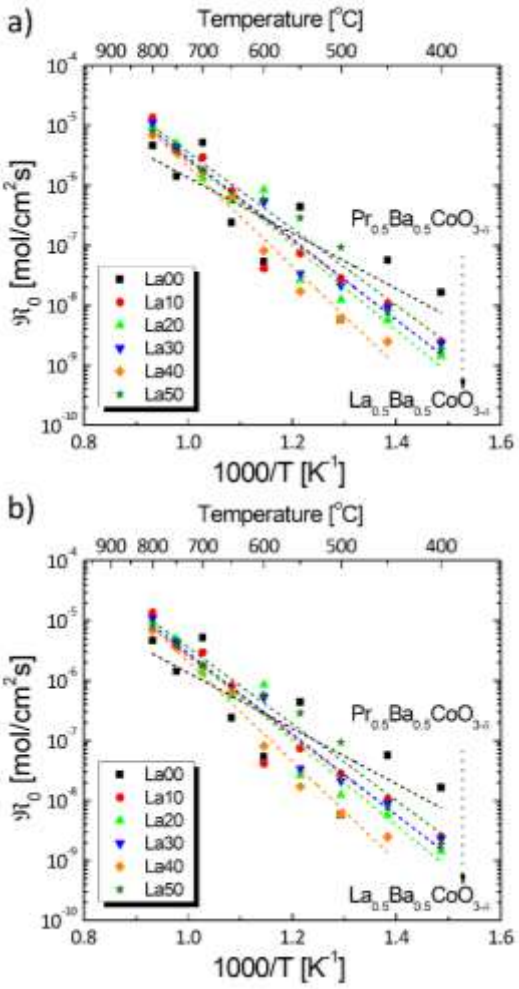

Figure 8: Arrhenius plot of a) $\mathbf{D}_{chem}$ and b) $\Re o$. Reference values at 600 and 700 °C and activation energies are listed at Table 2.

Table 2: Values of D_{chem} and k_{chem} at 600 and 700 ºC in air and its activation energies for all samples.

Sample	*600 ºC*		*700 ºC*		E_a^D[eV]			E_a^k [eV]		
	D_{chem} [cm2/s]	k_{chem} [cm/s]	D_{chem} [cm2/s]	k_{chem} [cm/s]						
La00	$1.6\ 10^{-9}$	$2.8\ 10^{-5}$	$6.2\ 10^{-8}$	$1.7\ 10^{-4}$	1.1	±	0.2	0.9	±	0.2
La10	$1.5\ 10^{-7}$	$8.7\ 10^{-6}$	$3.6\ 10^{-7}$	$7.7\ 10^{-5}$	0.8	±	0.2	1.3	±	0.1
La20	$6.4\ 10^{-8}$	$2.1\ 10^{-5}$	$1.3\ 10^{-6}$	$9.7\ 10^{-5}$	0.7	±	0.1	1.4	±	0.1
La30	$3.6\ 10^{-7}$	$1.6\ 10^{-5}$	$1.5\ 10^{-6}$	$1.1\ 10^{-4}$	0.72	±	0.07	1.34	±	0.09
La40	$5.7\ 10^{-8}$	$5.1\ 10^{-5}$	$1.1\ 10^{-7}$	$9.3\ 10^{-6}$	0.65	±	0.06	1.65	±	0.09
La50	$2.2\ 10^{-7}$	$1.6\ 10^{-5}$	$1.8\ 10^{-6}$	$7.6\ 10^{-5}$	0.89	±	0.02	1.27	±	0.08

Life Testing

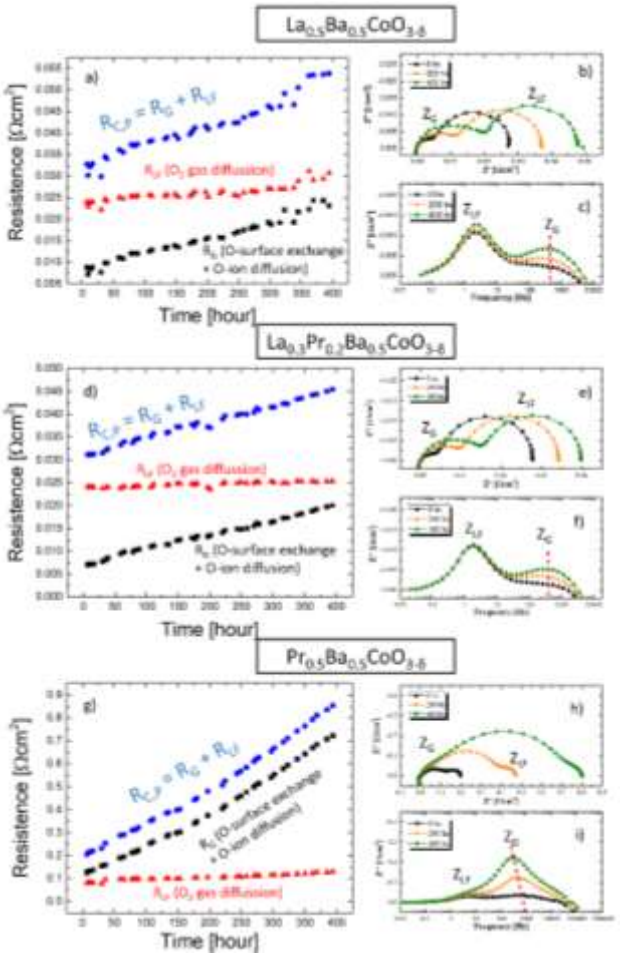

Figure 9: a) Evolution of $R_{C,P}$, R_G and R_{LF} values with aging time for La50 sample at 700 °C in air. b) and c) Nyquist and Bode plots obtained for La50 sample at 0, 200 and 400 h. d), e) and f) show the same information for La30 sample and g), h) and i) for La00. Dashed red lines in figure c, f and I are a guide to the eyes showing the evolution with time of the maximum frequency of R_G.

Figures 9.a), d) and g) show the time evolution of R_G, R_{LF}, and the total polarization resistance $R_{C,P}$ measured by EIS at 700 °C in air as a function of time, for the La50, La 30 and La00 electrodes, respectively. The results reveal an increase, after 400 hours, of the total polarization resistance between 45 % and 64 % for samples that have a combination of cubic and tetragonal phases and an increase of ~ 316 % for the sample with tetragonal phase. **Error! Reference source not found.** contains information about the overall rate of change over the aging, defined as $\frac{1}{R^0_{C,P}}\frac{dR_{C,P}}{dt}$, and the rate of change for $R_{LF}\left(\frac{1}{R^0_{LF}}\frac{dR_{LF}}{dt}\right)$ and $R_G\left(\frac{1}{R^0_G}\frac{dR_G}{dt}\right)$. As can be observed from Figure 9, the low frequency contribution (R_{LF}), associated to O_2 gas diffusion, is the main contribution to the polarization resistance at 700 ºC in air for samples with mixing cubic and tetragonal phases. The change of R_{LF} with time is negligible compared with the evolution of R_G for all samples (see Table 3). The little increase of R_{LF} can be attributed to the particle coarsening reported in Table 1 which reduces the pore fraction ($\varepsilon_P = 1 - \varepsilon$) and increases the pore phase tortuosity (τ_p) - i.e.$R_{LF} \propto \frac{\tau_p}{\varepsilon_p}$ [25] supporting an increasing of 5% of O_2 gas diffusion polarization resistance. On the contrary, the increases of R_G cannot be totally explained by the reduction of the specific surface area - i.e. $R_G \propto \frac{1}{\sqrt{a}}$ [25]. It can be noted from the Nyquist and Bode plots (Figure 9) and from **Error! Reference source not found.** that the pure tetragonal phase (La00), at difference of that observed for La30 and La50, not only shows a highest increasing of its R_G resistance but also its time constant τ_G, became slower with time suggesting a different degradation mechanism for the tetragonal phase. The ohmic resistances (not shown here) remains constant with time, indicating thermal compatibility at the electrode/electrolyte interface.

Table 3: Rates of change for $R_{Total}\left(\frac{1}{R^0_{C,P}}\frac{dR_{C,P}}{dt}\right)$, $R_{LF}\left(\frac{1}{R^0_{LF}}\frac{dR_{LF}}{dt}\right)$ and $R_G\left(\frac{1}{R^0_G}\frac{dR_G}{dt}\right)$ after 400 hours. The percent of change for each contribution is indicated between parentheses.

Sample	$\frac{1}{R^0_{C,P}}\frac{dR_{C,P}}{dt}$	$\frac{1}{R^0_{LF}}\frac{dR_{LF}}{dt}$	$\frac{1}{R^0_G}\frac{dR_G}{dt}$
La00 (tet)	0.008 h^{-1} (~ 316 %)	0.002 h^{-1} (~ 63 %)	0.01 h^{-1} (~ 477 %)
La30 (cub + tet)	0.001 h^{-1} (~ 46 %)	0.0001 h^{-1} (~ 5 %)	0.005 h^{-1} (~ 86 %)
La50 (cub + tet)	0.002 h^{-1} (~ 64 %)	0.0007 h^{-1} (~ 28 %)	0.004 h^{-1} (~ 63 %)

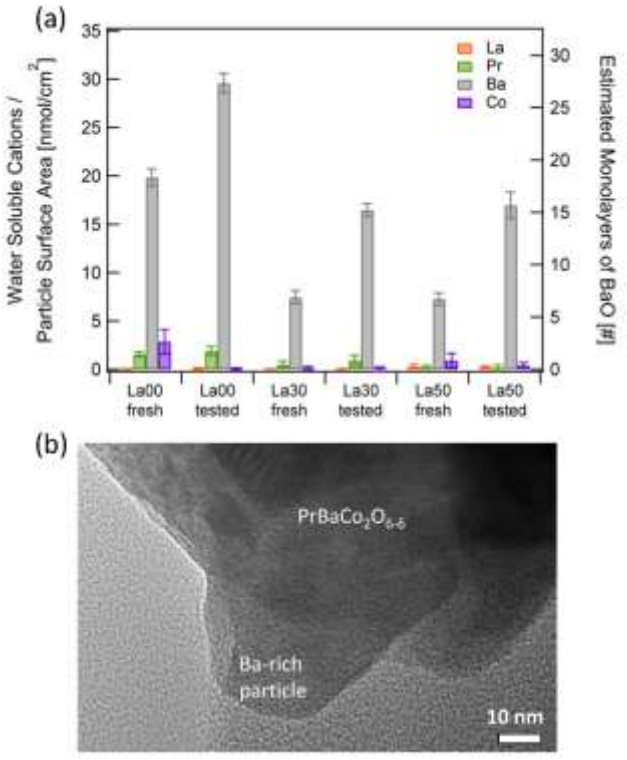

Figure 10: (a) Amounts of water-soluble cations detected by ICP-OES. The cation amounts were normalized to LPBC surface area, obtained by 3D FIB-SEM as shown in Table 1. (b) HR-TEM image showing the formation of a typical ~20 nm Ba-rich segregated particle on the perovskite surface according to EDS analysis.

The amount of water-soluble cations (Ba, La, Pr and Co) on the electrode surfaces, before (fresh) and after 400 h (tested) of the La00, La30 and La50 life test, was measured using ICP measurements. The estimated amount, represented as BaO monolayers, was also indicated in Figure 10. The highest value of Ba surface concentration in comparison with the other cations indicates a Ba surface segregation during sample processing in all samples, but especially for the tetragonal phase (La00), where the estimated number of monolayers in the fresh sample is more than twice that for La30 and La50. Also, Figure 10 (a) shows that the amount of Ba in the surface increases a 100% after the test for La30 and La50, but for the La00 sample it amounts increase only ~ 50 %. The study of perovskite surface by HR-TEM and EDS indicate that Ba segregation consists in the formation of ~ 20 nm Ba-rich particles on the perovskite surface (see Figure 10 b). Summarizing, La00 with tetragonal phase shows the highest value of R_G at the beginning of the life testing as well as the largest Ba surface concentration, however whereas the R_G time evolution is also the most significant phenomena, the Ba surface segregation is not. After comparing these results with previous works where the Sr-surface segregation was evaluated for the $La_{0.6}Sr_{0.4}Co_{0.2}Fe_{0.8}O_{3-\delta}$ cathode [31], it can be observed a larger cation surface segregation in these Ba-based cathodes- i.e. Ba surface concentration is duplicated in the half of time that Sr concentration. However, unlike what was observed in the case of Sr-segregation in the $La_{0.6}Sr_{0.4}Co_{0.2}Fe_{0.8}O_{3-\delta}$ cathodes [31], where both kinetic parameters decrease about a 50% for the aged sample, the diffusion and surface exchange coefficients show dissimilar behavior for $La_{0.5-x}Pr_xBa_{0.5}CoO_{3-\delta}$ series. Table 4 shows, from the analysis of the values of $\boldsymbol{D_{chem}}$ and $\boldsymbol{k_{chem}}$ as a function of the aging time, that the increase of R_G in LPBC series is mainly due to the decrease of $\boldsymbol{D_{chem}}$ (~-100%) and not to $\boldsymbol{k_{chem}}$ that increases (+66%, La50) or remains approximately constant (-6%, La30) for the samples with mixed cubic and tetragonal phases. While there is a consensus in the literature to associate the degradation of the polarization resistance to the fact that the segregation of SrO species blocks the surface exchange process [32], the effect of Ba-segregation is not entirely clear. A few works studying the effect of $BaCO_3$ nanoparticles decorating the surface of LSCF [33] and LSF [34] cathodes demonstrated that Ba ions improve the chemical oxygen surface exchange coefficients may be due to that barium ions on the surface play a key role in the adsorption of oxygen molecules and the formation/decomposition of intermediates [35]. The coexistence of both effects could explain an optimum amount of Ba in the surface to be the reason of different time evolution behavior observed for $\boldsymbol{k_{chem}}$, being more important the blocking effect in the tetragonal sample as is evident for the reduction of the time constant τ_G (see Figure 9.i). On other hand, because the pO_2 dependence of $\boldsymbol{D_{chem}}$ suggested a bulk mechanism for ion diffusion, it is reasonable to assume that the decreasing of the diffusion coefficient $\boldsymbol{D_{chem}}$ could be associated to a negative impact of the Ba depletion in the sub-surface region naturally accompanying the Ba-surface segregation which could produce a local lattice distortion affecting the O-ion transport. This Ba segregation could be controlled and reduced as in the case of Sr segregation. Recent work showed that Sr segregation on LSCF slows substantially with decreasing temperature [36], it is possible that our electrodes would be stable enough if operated at 500 – 600 ºC. Tomov demonstrated that composite cathodes decorated with GDC nanoparticles showed stable operation after aging assigned to the suppression of SrO segregation by the GDC nano-decoration [37]. This kind of strategy could be also useful to mitigate Ba surface segregation in these materials.

Table 4: Values of $\boldsymbol{D_{chem}}$ and $\boldsymbol{K_{chem}}$ at 700 ºC in function of aging time for La50, La30 and La00 samples.

Time [h]	La50		La30		La00	
	$\boldsymbol{D_{chem}}$**[cm²/s]**	$\boldsymbol{k_{chem}}$ **[cm/s]**	$\boldsymbol{D_{chem}}$**[cm²/s]**	$\boldsymbol{k_{chem}}$ **[cm/s]**	$\boldsymbol{D_{chem}}$**[cm²/s]**	$\boldsymbol{k_{chem}}$ **[cm/s]**
0	$1.4\ 10^{-5}$	$5.5\ 10^{-5}$	$7.0\ 10^{-6}$	$1.1\ 10^{-4}$	$4.7\ 10^{-9}$	$1.7\ 10^{-4}$
220	$2.0\ 10^{-6}$	$7.9\ 10^{-5}$	$2.2\ 10^{-6}$	$9.2\ 10^{-5}$	$6.3\ 10^{-10}$	$1.5\ 10^{-4}$
400	$7.8\ 10^{-7}$	$9.1\ 10^{-5}$	$9.8\ 10^{-7}$	$1.0\ 10^{-4}$	$3.0\ 10^{-10}$	$1.0\ 10^{-5}$
Percent of Change	-94%	66%	-86%	-6%	-94%	-39%

Conclusions

A soft chemical route was used to obtain $La_{0.5-x}Pr_xBa_{0.5}CoO_{3-\delta}$ (LPBC) powders. The samples present a mixture of phases: cubic + tetragonal with the exception of those that contain low lanthanum content that have a tetragonal crystalline structure as a single phase. The study of electrode performance by EIS as a function of temperature, pO_2 and time suggested that two processes contribute to $R_{C,P}$:

1) The low frequency resistance (R_{LF}), which is associated to O_2 gas diffusion. This contribution dominates the cathode polarization resistance as T increases or pO_2 decreases in samples with a mixture of phases but it represents the smallest contribution to $R_{C,P}$ in tetragonal samples. The O_2 gas transport resistance shows little changes with time which is in agreement with small change of microstructure.

2) The high frequency Gerischer-resistance (R_G), which can be modeled by using the ALS approximation. This R_G considers that the O_2-reduction reaction is co-limited by O-surface exchange and O-ion diffusion. By the analysis of the dependence of O-ion chemical diffusion ($\boldsymbol{D}_{chem}$) and the surface exchange rate ($\mathcal{R}o$) with temperature and pO_2 is concluded that the surface process is dominated by surface dissociation or surface dissociative adsorption, according to Adler's model, and that the O-ion diffusion mechanism is dominated by bulk transport. This mechanism is mostly determined by the crystal structure, microstructure and surface conditions. The R_G is the contribution showing the largest evolution with time and, unlike samples with high lanthanum content, it dominates the cathode polarization resistance for sample with tetragonal phase.

Ageing of LPBC symmetric-electrode cells with GDC electrolytes, carried out at 700 ºC for 400 hours in air, resulted in an increase of the electrode polarization resistance by about ~ 50 % for samples with two phases and an increase of ~ 316 % for the sample with tetragonal phase. 3D tomographic analysis indicated no significant changes in the selected microstructural parameters due to ageing. ICP-OES measurements of selectively dissolved surface species shows that the amount of surface Ba in tasted samples was increased on all cases. This increase of Ba concentration at the surface caused a decrease of $\boldsymbol{D}_{chem}$ (-100%) which would be associated with a detriment in the O-ions diffusion, due to local lattice distortion associated to the Ba depletion in the sub-surface region. The variation of $\boldsymbol{k}_{chem}$ due to the Ba surface concentration could be attributed to two opposing phenomena: first, the segregation of Ba ions forms BaO or BaCO species which blocks the surface exchange sites on the LPBC surface but at the same time can could contribute to the formation/decomposition of intermediates in the adsorption of oxygen molecules. All samples present a coexistence of this two phenomena being the blocking process more important in tetragonal samples and less significant when the lanthanum content increases.

Finally, the $La_{0.5-x}Pr_xBa_{0.5}CoO_{3-\delta}$ cathodes with an unique microstructure intimately mixing cubic and tetragonal phases (La-rich compound), exhibit a low polarization resistance taking values around 0.15 and 0.04 Ωcm^2 at 600 and 700 ºC in air, respectively. As T increases the cathode polarization is dominated by the O_2 gas diffusion (~ 50% of the $R_{C,P}$ in air), whereas the "true electrode" response associated to a Gerischer-impedance and modeled by the Adler-Lane-Steele model just contributed with R_G values around 0.08 and 0.015 Ωcm^2 at 600 and 700 ºC in air, respectively. These La-rich cathodes are also those showing the lower degradation rate, being the more important impact of the Ba surface segregation a decreasing of the O-ion bulk diffusion whereas the O-surface exchange shown a positive effect increasing the surface exchange coefficient with time.

Conflicts of interest

There are no conflicts to declare.

Acknowledgements

Authors want to acknowledge the support of CONICET-NSF collaborative project, AGNPCyT PICT2016-2965 and CONICET PIP 2015 0565. This work has been supported by the Brazilian Synchrotron Light Laboratory (LNLS, CNPEM, Brazil) under Research Proposal D10B-XPD-20150226. The authors also acknowledge the assistance of the Electron Probe Instrumentation Center (EPIC) at the NUANCE Center-Northwestern University, which has received support from the MRSEC program (NSF DMR-1121262) at the Materials Research Center; the International Institute for Nanotechnology (IIN); and the State of Illinois, through the IIN. Metal analysis was performed at the Northwestern University Quantitative Bio-element Imaging Center.

.

Notes and references

1 Z. Gao, L.V. Mogni, E.C. Miller, J.G. Railsback, S.A. Barnett, *Energy Environ. Sci.*, 2016, **9**, 1602.
2 Z. Shao, S.M. Haile, *Nature*, 2004, **431**, 170.
3 S.P. Simner, M.D. Anderson, M.H. Engelhard, J.W. Stevenson, *Electrochem. Solid-State Lett.*, 2006, **9**, A478.
4 W. Lee, J.W. Han, Y. Chen, Z. Cai, B. Yildiz, *J. Am. Chem. Soc.*, 2013, **135 (21)**, 7909.
5 R. Merkle, Y.A. Mastrikov, E.A. Kotomin, M.M. Kuklja, J. Maier, *J. Electrochem. Soc.*, 2012, **159**, B219.
6 D.N. Mueller, R. De Souza, T.E. Weirich, D. Roehrens, J. Mayer, M. Martin, *Phys. Chem. Chem. Phys.*,2010, **12**, 10320.
7 S. Švarcová, K. Wiik, J. Tolchard, H.J.M. Bouwmeester, T. Grande, *Solid State Ionics*, 2008, **178**, 1787.
8 K. Efimov, Q. Xu, A. Feldhoff, *Chem. Mater.*, 2010, **22**, 5866.
9 S. Yakovlev, C.Y. Yoo, S. Fang, H.J.M. Bouwmeester, *Appl. Phys. Lett.*, 2010, **96**, 2008.
10 D. Garcés, A. L. Soldati, H. Troiani, A. Montenegro-Hernández, A. Caneiro,L. V. Mogni, *Electrochimica Acta*, 2016, **215**, 6.
11 S. Pang, X. Jiang, X. Li, Z. Su, H. Xu, Q. Xu, C. Chen, *Int. J. Hydrogen Energy.*, 2012, **37**, 6836.
12 R. Amin, K. Karan, *J. Electrochem. Soc.*, 2010, **157**, B285.
13 Lenser, C., et al., *Solid State Ionics*, 2018, **314**, 204.
14 Tuller, H.L., et al., *Solid State Ionics*, 2012, **225**, 194.
15 Ji, Y., et al., *Journal of Alloys and Compounds*, 2005, **389**, 317.
16 A. Caneiro, P. Bavdaz, J. Fouletier, J.P. Abriata, *Rev. Sci. Instrum.*, 1982, **53**, 1072.
17 A. Caneiro, M. Bonnat, J. Fouletier, *J. Appl. Electrochem.*, 1981, **11**, 83.
18 C. F. Setevich, L. V. Mogni, A. Caneiro, F. D. Prado, *Int. J. Hydrogen Energy.*, 2012, **37**, 14895.
19 L. Baqué, A. Caneiro, M.S. Moreno, A. Serquis, *Electrochem. Commun.*, 2008, **10**, 1905.
20 J. Park, J. Zou, H. Yoon, G. Kim, J.S. Chung, *Int. J. Hydrogen Energy.*, 2011, **36**, 6184.
21 J. H. Kim, J. T. S. Irvine, *Int. J. Hydrogen Energy.*, 2012, **37**, 5920.

22 A. C. Tomkiewicz, M. Meloni, S. McIntosh, *Solid State Ionics.*, 2014, **260**, 55.
23 K. Zhang, L. Ge, R. Ran, Z. Shao, S. Liu, *Acta Mater.*, 2008, **56**, 4876.
24 D. Marinha, L. Dessemond, J.S. Cronin, J.R. Wilson, S.A. Barnett, E. Djurado, *Chem. Mater.*, 2011, **23**, 5340.
25 S.B. Adler, J.A. Lane, B.C.H. Steele, *J. Electrochem. Soc.*, 1996, **143**, 3554.
26 S.B. Adler, *Solid State Ionics.*, 1998, **111**, 125.
27 Y. X. Lu, C. Kreller, S.B. Adler, *J. Electrochem. Soc.*, 2009, **156**, B513.
28 S. B. Adler, X.Y. Chen, J.R. Wilson, *J. Catal.*, 2007, **245**, 91.
29 R. A. De Souza, *Phys. Chem. Chem. Phys.*, 2006, **8**, 890.
30 K. Yakal-Kremski, L. V Mogni, A. Montenegro-Hernández, A. Caneiro, S. A. Barnett, *J. Electrochem. Soc.*, 2014, **161**, 1366.
31 H. Wang, K. J. Yakal-Kremski, T. Yeh, G.M. Rupp, A. Limbeck, U. Fleig, S.A. Barnett, *J. Electrochem. Soc.*, 2016, **163**, 581.
32 Z. Cai, M. Kubicek, J. Fleig, B. Yildiz, *Chem. Mater.*, 2012, **24**, 1116.
33 T. Hong, S. Lee, P. Ohodnicki, K. Brinkman, *Int. J. Hydrogen Energy*, 2017, **42,** 24978.
34 T. Hong, F. Chen, C. Xia, *J. Power Sources.*, 2015, **278**, 741.
35 X. Cao, T. Hong, R. Yang, J. H. Tian, C. Xia, J. C. Dong, J. F. Li, J. *Phys. Chem. C.*, 2016, **120**, 22895.
36 H. Wang, S.A. Barnett, *ECS Transactions*, 2017, **78**, 905.
37 R.I.T. Tom, M. Williams, C. Gao, B.A. Glowacki, *J. Appl. Electrochem.*, 2017, **47**, 641.